



Structural changes in C–S–H gel during dissolution: Small-angle neutron scattering and Si-NMR characterization



Ana Trapote-Barreira^{a,*}, Lionel Porcar^{b,c}, Jordi Cama^a, Josep M. Soler^a, Andrew J. Allen^b

^a Institute of Environmental Assessment and Water Research (IDAEA), Barcelona 08034, Catalonia, Spain

^b National Institute of Standards and Technology (NIST), Gaithersburg, MD 20899, USA

^c Large Scale Structure Group, Institut Laue Langevin, Grenoble, France

ARTICLE INFO

Article history:

Received 28 August 2014

Accepted 11 February 2015

Available online 7 March 2015

Keywords:

Calcium-Silicate-Hydrate (B)
Small-Angle X-Ray Scattering (B)
Cement (D)
Modeling (E)
Dissolution

ABSTRACT

Flow-through experiments were conducted to study the calcium–silicate–hydrate (C–S–H) gel dissolution kinetics. During C–S–H gel dissolution the initial aqueous Ca/Si ratio decreases to reach the stoichiometric value of the Ca/Si ratio of a tobermorite-like phase (Ca/Si = 0.83). As the Ca/Si ratio decreases, the solid C–S–H dissolution rate increases from $(4.5 \times 10^{-14}$ to $6.7 \times 10^{-12})$ mol m⁻² s⁻¹. The changes in the microstructure of the dissolving C–S–H gel were characterized by small-angle neutron scattering (SANS) and ²⁹Si magic-angle-spinning nuclear magnetic resonance (²⁹Si-MAS NMR). The SANS data were fitted using a fractal model. The SANS specific surface area tends to increase with time and the obtained fit parameters reflect the changes in the nanostructure of the dissolving solid C–S–H within the gel. The ²⁹Si MAS NMR analyses show that with dissolution the solid C–S–H structure tends to a more ordered tobermorite structure, in agreement with the Ca/Si ratio evolution.

© 2015 Elsevier Ltd. All rights reserved.

1. Introduction

Portland cement concrete is used worldwide to build all types of constructions with different purposes. Houses, factories, bridges, storage facilities, etc. are examples of cement-based structures. In particular, concrete is the predominate material in engineered barriers in low-level nuclear waste disposal facilities [1]. A combination of diffusion-transport effects and chemical reactions promotes the alteration of the microstructure of the material when subject to a flow of water: dissolution of cement constituents such as portlandite (calcium hydroxide, denoted CH in cement notation) and calcium silicate hydrate (C–S–H). The C–S–H gel, which constitutes at least 60% of the fully hydrated cement paste by volume, is the main strength-giving phase, also responsible for the durability and radionuclide barrier properties of cement owing to the features of its microstructure (porous structure and alkaline solution inside the pores that limit the solubility of radionuclides [2,3]). In this context, there is a need to study any alteration of the microstructure of the cement, together with any associated changes in the C–S–H gel microstructure caused by the presence of water.

In recent years, considerable research on cement degradation has been conducted to understand the relevant mechanisms governing this complex process. The complexity and demanding nature of this research has required several different methodologies and techniques to be applied. A common methodology, used due to its simplicity, is based on laboratory leaching experiments (i.e., closed systems) in which decalcification of the solid C–S–H microstructure within the gel (after dissolution of CH) and consequent changes in the cement mechanical properties are studied [4–9]. Among the techniques used to study the cement and concrete structures, ²⁹Si magic-angle-spinning nuclear magnetic resonance (²⁹Si MAS-NMR) and small-angle neutron scattering (SANS) are particularly useful for investigating porous structures like C–S–H gel, given that the amorphous nature of C–S–H renders diffraction ineffective. In addition, specimens can be studied in their natural saturated state, thus avoiding complications associated with drying the C–S–H gel [8]. SANS data are effective in probing features in the 10 Å to 1000 Å (1 nm to 100 nm) size range (short-ranged crystalline order) that defines critical aspects of the solid C–S–H structure within the gel [7], providing quantitative information about microstructural features (e.g., particle size, shape, surface area and fractal properties). SANS covers the range of scattering q values from 0.002 \AA^{-1} to 0.2 \AA^{-1} , where $q = (4\pi/\lambda)\sin(\theta)$, λ is the neutron wavelength and 2θ is the scattering angle. SANS data permit determination of the fractal exponent and fractal morphology of the C–S–H gel over a large scale range, and this can be quantified through application of a fractal microstructure model [8,10–14].

* Corresponding author at: Jordi Girona 18-26, Barcelona 08034, Catalonia, Spain. Tel.: +34 934006100.

E-mail address: anatraptotebarreira@gmail.com (A. Trapote-Barreira).

In this study powdered C–S–H gel samples were dissolved for up to 74 days in Milli-Q¹ water (18.2 MΩ · cm at 25 °C) using flow-through reactors, under a CO₂-free atmosphere at room temperature (23 ± 2) °C. The evolution of the C–S–H gel dissolution with time was monitored by the solution chemistry variation as it was performed by Trapote-Barreira et al. [15]. In parallel, the reacted C–S–H gel samples were characterized using the ²⁹Si-NMR and SANS techniques to evaluate the changes in the dissolving solid C–S–H nanostructure (particle size, shape, surface area and fractal exponents). The SANS contrast matchpoint of the starting solid C–S–H was obtained from the measured change in the scattering contrast as a function of D₂O content. The content of both solid C–S–H and fine CH crystals from the initial composition of C–S–H gel was evaluated. This combined approach allowed investigation of the changes in structure of the C–S–H gel related to changes in solution composition with time. The advantage of this kinetic approach is that it yields a full understanding of the overall C–S–H gel-dissolution reaction, and contributes to the assessment of cement durability.

2. Experimental methodology

2.1. Sample characterization

The starting cement paste sample (prior to dissolution) was obtained from hydration of 3CaO · SiO₂ (C₃S) using a water/C₃S ratio of 0.5 by mass for 120 days under a CO₂-free atmosphere (N₂ atmosphere) in a glove box. The resulting paste was dried with isopropanol and ground in a glove box to obtain powdered samples with powder grain particles ranging in size from 10 μm to 100 μm (see more details in Trapote-Barreira et al.) [15]. X-ray diffraction (XRD) measurements of the hydrated paste were performed with a Bruker D-5005 diffractometer using Cu K-α1 radiation (λ = 1.5406 Å) at 40 kV and 30 mA. The range of 2θ scanning was from 4° to 60°; scan step and step duration were 0.05° and 3 s, respectively. The powder XRD patterns showed peaks for portlandite, quartz and calcite. XRD could not detect the presence of C₃S. Rietveld analyses of the XRD pattern associated with these phases [16] allowed us to deduce the amount of (non-crystalline) C–S–H, within the starting sample, which was found to consist of 67% mass C–S–H, 27.5% mass portlandite, 1.5% mass quartz and 4% mass calcite, the latter due to some sample carbonation. This is in agreement with the amount of C–S–H and CH expected from the C₃S hydration reaction (67% mass C–S–H and 33% mass portlandite). The specific surface area of the starting hydrated paste sample was measured using the 5-point BET (N₂) method; the BET surface area was (11.7 ± 1.7) m² g⁻¹. Scanning Electron Microscopy in combination with Energy Dispersive X-ray Spectroscopy (SEM-EDX) showed that the samples consisted of aggregates of particles of C–S–H and CH. A portion of the starting C–S–H gel was mounted in resin and polished for electron microprobe (EM) analyses that were performed on multiple points using a CAMECA SX50 microprobe under a 20 kV accelerating potential and 20 nA beam current. EM showed that the starting C–S–H gel was compositionally homogeneous at a spatial resolution of about 2 μm. Three different ranges of Ca/Si ratio existed in the measured powder grain particles: (1) Ca/Si ratio between 1.68 and 1.8, corresponding to solid C–S–H; (2) Ca/Si ratio between ≈ 1.8 and 2.34, corresponding to nanoscale C–S–H particles co-existing with a small fraction of nanoscale CH; and (3) Ca/Si ratio larger than 6, indicative of microscale portlandite crystals.

¹ Cement nomenclature used: C = CaO, S = SiO₂, H = H₂O, D = D₂O.

Certain commercial materials and equipment are identified in this paper only to specify adequately the experimental procedure. In no case does such identification imply recommendation by NIST nor does it imply that the material or equipment identified is necessarily the best available for this purpose.

2.2. Dissolution experiments

Powder samples of the starting hydrated paste with mass between 1.5 g and 3.0 g and powder particle size ≈ 10 μm were placed in the flow-through reactors under CO₂-free atmospheric conditions and room temperature (23 ± 2) °C (Fig. A1). These masses were sufficient to allow us to retrieve enough reacted sample to perform BET, ²⁹Si-NMR, XRD and SANS measurements. Table 1 details the conditions for each dissolution flow experiment in terms of duration, flow rate, initial total solid mass (C–S–H and CH) and initial solid C–S–H mass deduced to be present (see details of the setup in Trapote et al. [15]). Milli-Q water (18.2 MΩ · cm at 25 °C) reacted with the starting C–S–H gel, while being supplied at a constant flow rate over the course of the experiment. The flow rates were increased from 0.040 mL min⁻¹ to 0.126 mL min⁻¹ shortening residence times from ≈ 16 h to 5 h. The output solutions were periodically collected. The evolution of the dissolution reaction with time was monitored by measuring the output solution pH and the output aqueous concentrations of Ca and Si, which were released from the dissolution of the C–S–H and portlandite. Variation of Ca/Si ratio with time was determined from the periodical variation in the Ca and Si output concentrations [15]. Experiments with different mass and flow rate were repeated with different time durations (from 16 days to 74 days) to evaluate changes in the solid composition with time. Therefore, steady-state conditions were not always reached.

The input and output solution pH was measured at 25 °C using a Thermo Orion Ag/AgCl electrode. Calibration was made with Crison © standard buffer solutions of pH 7.00 (sodium phosphate and potassium phosphate) and pH 9.21 (borax). The uncertainty was 0.1 pH units for solutions with pH higher than 11 and 0.05 for solutions between 11 and 10. After the pH measurements, output solutions were acidified to pH 3 to prevent precipitation of calcium carbonate in the solutions. Total concentrations of Ca and Si of the output solutions were analyzed by Inductively Coupled Plasma Atomic Emission Spectroscopy (ICP-AES, thermo Jarrel-Ash with CID detector and a Perkin Elmer Optima 3200RL). The accuracy of ICP-AES measurements was estimated to be around 3%. The detection limit of the analysis for Ca and Si concentration was 0.5 ppm. Based on a simple mass balance equation, the dissolution rate (mol m⁻² s⁻¹), R, in a flow-through experiment is given by [17]:

$$R = \frac{dc_i}{dt} \cdot \frac{V}{m \cdot S \cdot v_i} + q_v \frac{(c_i - c_i^0)}{m \cdot S \cdot v_i} \quad (1)$$

where, c_i and c_i^0 (mol m⁻³) represent the out- and in-flowing concentrations of the i th element, v_i is the stoichiometry coefficient of the i th

Table 1
Experimental conditions of the flow-through experiments.

Experiment	Time (day)	Flow rate (mL min ⁻¹)	Mass	
			(C–S–H gel + CH) (g)	C–S–H gel
C–S–H-1	16	0.126	3.0000	2.0100
C–S–H-2	16	0.046	1.5000	1.0050
C–S–H-3	16	0.054	3.0000	2.0100
C–S–H-4	17	0.041	2.9013	1.9497
C–S–H-5	31	0.042	1.5039	1.0076
C–S–H-6	44	0.054	2.9934	2.0116
C–S–H-7	67	0.097	2.9980	2.0147
C–S–H-8	74	0.041	2.9951	2.0127

Experiments are ordered according to their duration.

C–S–H gel mass is 67% of that of C–S–H + CH mass.

C–S–H-4, C–S–H-6, C–S–H-7 and C–S–H-8 experiments are the same as C–S–H-25-10, C–S–H-25-9, C–S–H-25-18 and C–S–H-25-8 from [15], respectively.

element in the studied mineral, V is the volume of the reaction cell (m^3), q_v ($\text{m}^3 \text{s}^{-1}$) is the fluid volume flux through the reactor, m is the mass of mineral (g), and S ($\text{m}^2 \text{g}^{-1}$) is the specific (BET measured) surface area of the mineral. In the experiments where the composition of the output solutions did not reach a constant value, the dissolution rate was calculated from the last output concentration. The dissolution rate in the experiments where the composition of the output solution reaches a constant value ($dc_i/dt = 0$), i.e., the steady-state output concentration, is readily calculated from the second term on the right of the previous equation:

$$R_i = q_v \frac{(c_i - c_i^0)}{m \cdot S \cdot v_i} \quad (2)$$

Dissolution rates (R_i) were only calculated based on the Si output concentrations and normalized to both the final mass (R_{Si} expressed $\text{mol g}^{-1} \text{s}^{-1}$) and the final surface area (R_{Si} expressed in $\text{mol m}^{-2} \text{s}^{-1}$). The uncertainty associated with the calculated dissolution rate was estimated using the Gaussian uncertainty propagation method [18] to have a standard deviation uncertainty of 15% (1σ).

The powder samples from these experiments were retrieved after the dissolution reaction times specified in Table 1, and the measured final BET surface areas ranged from $14.5 \text{ m}^2 \text{g}^{-1}$ to $63.3 \text{ m}^2 \text{g}^{-1}$, which represents an increase in the reactive surface area by a factor of between 1.5 and 6 relative to the initial BET surface area, as shown in Table 2. Initial and retrieved powders were dried with isopropanol under a CO_2 -free atmosphere and examined by SEM in order to identify the major residual phases (C–S–H and CH) and characterize their morphology, and by XRD and Rietveld Analysis to quantify their content. ^{29}Si -NMR and SANS analyses were performed to determine the structural variation and examine the evolution of the surface area and morphology of the C–S–H gel within the powdered paste sample.

2.3. ^{29}Si MAS-NMR

The ^{29}Si MAS-NMR spectra of approximately 2 mg of cement paste sample (prior to dissolution) and reacted powder samples that underwent different degrees of dissolution were recorded on a Bruker Avance 400 NMR spectrometer (field strength of 9.4 T, Bruker Biospin AG, Fällanden, Switzerland) at 79.49 MHz applying 4.5 kHz spinning rates on a 7 mm CP MAS probe using ZrO_2 rotors. Single-pulse experiments were carried out by applying 30° pulses of 2.9 ms with ^1H decoupling of 31.3 kHz (TPPM15) and recycle delays of 20 s. The ^{29}Si chemical shift was referenced externally relative to tetramethylsilane at 0.0 ppm. The observed ^{29}Si resonances were

analyzed using the Q^n classification, where one Si tetrahedron is connected to n Si tetrahedra with n varying from 0 to 4 [19]. The relative proportions of silicon associated with the Q^n units were determined by the deconvolution of the spectra using the Dmfit program [20].

2.4. SANS

The SANS experiments were performed on powder samples of unreacted (starting) and reacted C–S–H gel, taken from the flow-through experiments at room temperature in a CO_2 -free atmosphere using the NG7 30-m SANS Instrument [21] at the NIST Center for Neutron Research (NCNR), Gaithersburg, Maryland, USA. The SANS neutron wavelength, λ , was 8.09 Å and using three different configurations of the instrument, the overall measured q range extended from 0.001 \AA^{-1} to 0.22 \AA^{-1} (0.01 nm^{-1} to 2.2 nm^{-1}). This q range is sufficient to characterize morphological features of particles with a size ranging from $\approx 10 \text{ \AA}$ to $\approx 1000 \text{ \AA}$. Scattered neutron intensities were recorded on a two-dimensional detector. These data were corrected for the background and empty-cell scattering and calibrated against a standard attenuator. The 2D SANS data set was reduced to 1D by circular averaging to obtain the scattered intensity or scattering cross-section ($d\Sigma/d\Omega$) as a function of the magnitude of the scattering vector, q [22]. At small scattering angles (small q values) the largest features are probed, whereas the smaller features are probed at higher q values. Owing to a decrease in SANS intensity with increasing q , the q upper limit to obtain scattering data from hydrated cement is just over 0.2 \AA^{-1} [23], as shown in Fig. 1.

To fit the scattered intensity data, a fractal microstructure model [8] was applied over the SANS q range where $q > 0.0035 \text{ \AA}^{-1}$. Below this q other non-fractal components dominate the scattering like micrometer-scale $\text{Ca}(\text{OH})_2$ [13]. Allen et al. [8] have shown that the model results confirm that the volume-fractal nature of hydrated cement is mainly attributable to the C–S–H component. This model combines the volume-fractal and the surface-fractal scattering terms (Appendix A). The former is attributed to random agglomeration of the outer-product C–S–H nanoparticles between grains, and the latter to deposition of the outer-product C–S–H nanoparticles at the clinker grain boundaries and on inert surfaces such as the micrometer scale CH crystallites. Also, the surface fractal may include some inner product formed topochemically [22]. The Irena program package [24], together with the model by Allen et al. [8], was used to analyze the SANS scattering data to obtain the solid C–S–H structure parameters: D_o , D_v , $\phi_{\text{C-S-H}}$, S_o , D_s , ξ_v and ξ_s , as well as the upper-limit volume fraction (ϕ_{MAX}), the fractally rough surface area (S_{SF}) and the surface area of the volume-fractal morphology (S_{VF}). Note that ϕ_{MAX} is defined as a measure of the total volume fraction occupancy of the volume-fractal phase. It is

Table 2
Experimental results of the flow-through experiments.

Experiment	Time (day)	pH out	Ca out (μM)	Si out	Aqueous Ca/Si	BET ($\text{m}^2 \text{g}^{-1}$)	Dissolution rate		Log R_{Si}
							R_{Si} ($\text{mol g}^{-1} \text{s}^{-1}$)	($\text{mol m}^{-2} \text{s}^{-1}$)	
C–S–H-1	16	10.96	735.6	12.93	56.88	14.5	1.36E-11	9.35E-13	–12.0
C–S–H-2	16	11.29	1824.9	4.05	450.56	52.7	3.11E-12	5.91E-14	–13.2
C–S–H-3	16	11.52	1748.04	4.26	409.88	18.6	1.89E-12	1.02E-13	–13.0
C–S–H-4	17	11.48	325.81	5.62	57.97	25.0	2.00E-12	7.90E-14	–13.1
C–S–H-5	31	11.09	1290.31	229.6	5.62	46.1	1.63E-10	3.54E-12	–11.5
C–S–H-6	44	10.74	375.55	6.09	61.62	63.3	2.77E-12	4.40E-14	–13.4
C–S–H-7	67	10.68	636.37	12.69	50.63	15.9	1.07E-11	7.10E-13	–12.1
C–S–H-8	74	10.21	694.91	388.89	1.80	61.7	1.40E-10	2.30E-12	–11.6

Aqueous Ca/Si ratio is computed from the Ca and Si output concentration (Ca out and Si out).

BET represents the measured specific surface area after the experiments (associated uncertainty is approximately 10%) (1σ).

Dissolution rate is calculated according to Eqs. (1) and (2). Log R_{Si} is calculated from dissolution rate expressed in $\text{mol m}^{-2} \text{s}^{-1}$.

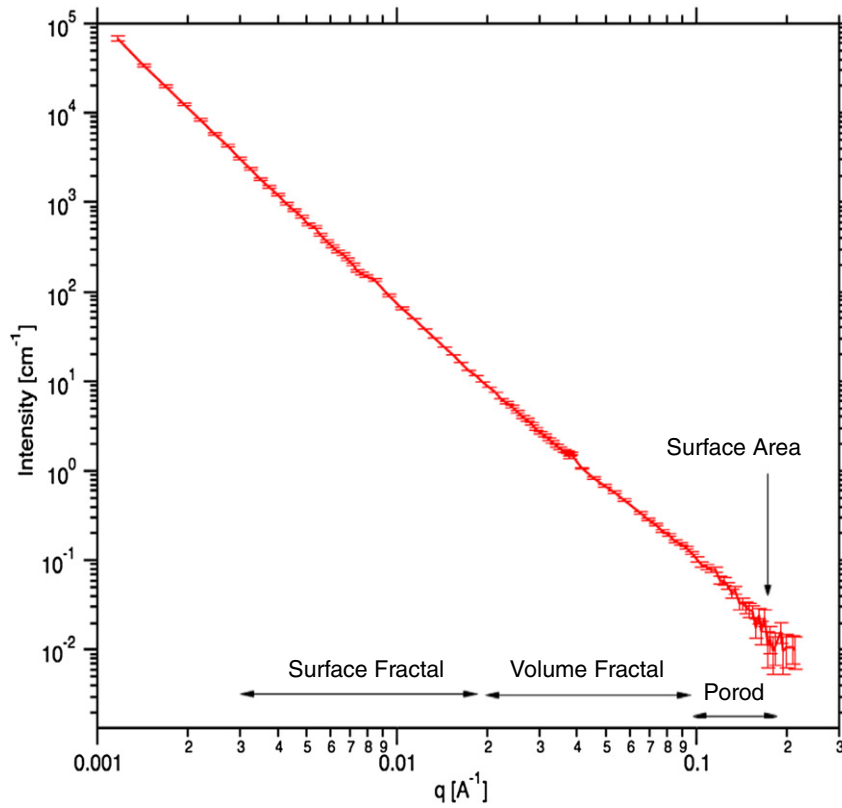


Fig. 1. Experimental SANS $I(q)$ data versus q for the starting cement paste sample (prior to dissolution) of this study. As the scattering vector (or angle) increases, scattering occurs from smaller features in the microstructure. Data plotted as a line the statistical uncertainties at each point.

necessarily a rough estimate based on $\phi_{MAX} = \phi_{C-S-H} \cdot ((\xi_V/R_C)^{(3-D_V)})$ and may be an over-estimate if the volume fractal structures actually grow into each other.

A set of six SANS experiments was carried out on the initial hydrated pastes prior to the dissolution measurements in order to obtain the contrast matchpoint (MP) of the starting solid C–S–H from the measured change in the scattering contrast as a function of D₂O content. 0.25 g of initial (unreacted) C–S–H gel sample was poured in 5 mL of mixed D₂O–H₂O solutions of 0%, 20%, 40%, 60%, 80% and 100% D₂O under CO₂-free atmospheric conditions in a N₂-filled glove box to avoid C–S–H carbonation. The mixtures were stirred for 12 h to ensure full exchange of H₂O and D₂O. Thomas et al. [6] showed that in thin cement specimens full H₂O–D₂O exchange occurs within hours. The relative scattering contrast was obtained by calculating the Porod constant (C_p) after plotting the SANS scattering data (Iq^4 versus q^4) in the Porod regime (q ranges from 0.11 to 0.2 Å⁻¹). The C_p values can be obtained from the unconstrained intercepts of linear fits of Iq^4 versus q^4 ,

and the flat background scattering, BGD, is obtained from the slopes as [6]:

$$I = \frac{C_p}{q^4} + BGD. \tag{3}$$

The highest C_p value obtained (0% of D₂O water) was used to normalize the derived C_p values at lower D₂O water (Table 3). In a two-phase system, such as pure C–S–H and water, the relative scattering contrast is a parabola with a minimum value of zero contrast at the MP [7]. The presence of an additional phase (e.g. CH) with a different contrast MP within the gel increases the minimum value in the C–S–H relative scattering contrast curve and displaces it with respect to D₂O content.

A second set of SANS experiments was performed with the reacted samples to study the changes in the C–S–H gel structure due to dissolution. According to the decreasing aqueous Ca/Si ratio and pH of the output solutions (Table 2), in the samples retrieved after 16 to 17 days, 31 to 44 days and 67 to 74 days, C–S–H and CH coexisted with a decrease in content of the latter. It is known that the CH contrast matchpoint occurs in a H₂O/D₂O fluid mixture of 31% D₂O [13]. Therefore, in a system with H₂O/D₂O fluid, C–S–H and CH, to obtain the relative scattering contrast of the C–S–H, solid samples must be mixed in a 31% of D₂O solution. No exchange between CH and D₂O is expected since these hydroxyl groups are bound into solid crystallites, while adsorbed water in C–S–H gel is. 0.25 g of each, unreacted and reacted samples from 16 to 74 days, were poured in 5 mL of solution (31% D₂O) for 24 h to allow full exchange of H₂O and D₂O. Based on the C–S–H gel dissolution rate [15] and portlandite solubility (22 mmol L⁻¹), the amount of C–S–H gel dissolved after 24 h is negligible compared to the amount of sample. Thereafter, sufficient

Table 3

C_p values (obtained from Porod scattering region) and the relative scattering contrast factor of initial hydrated C₃S paste with pore fluid.

% D ₂ O	C_p (10 ⁻¹² Å ⁻⁵)	Relative scattering contrast of initial C–S–H gel
0	0.69 ± 0.03	1
20	0.36 ± 0.02	0.53
40	0.18 ± 0.02	0.26
60	0.04 ± 0.01	0.06
80	0.03 ± 0.01	0.04
100	0.10 ± 0.01	0.14

Initial hydrated C₃S paste is composed of 67% mass of C–S–H, 27.5% mass of portlandite (CH), 1.5% mass quartz and 4% mass calcite.

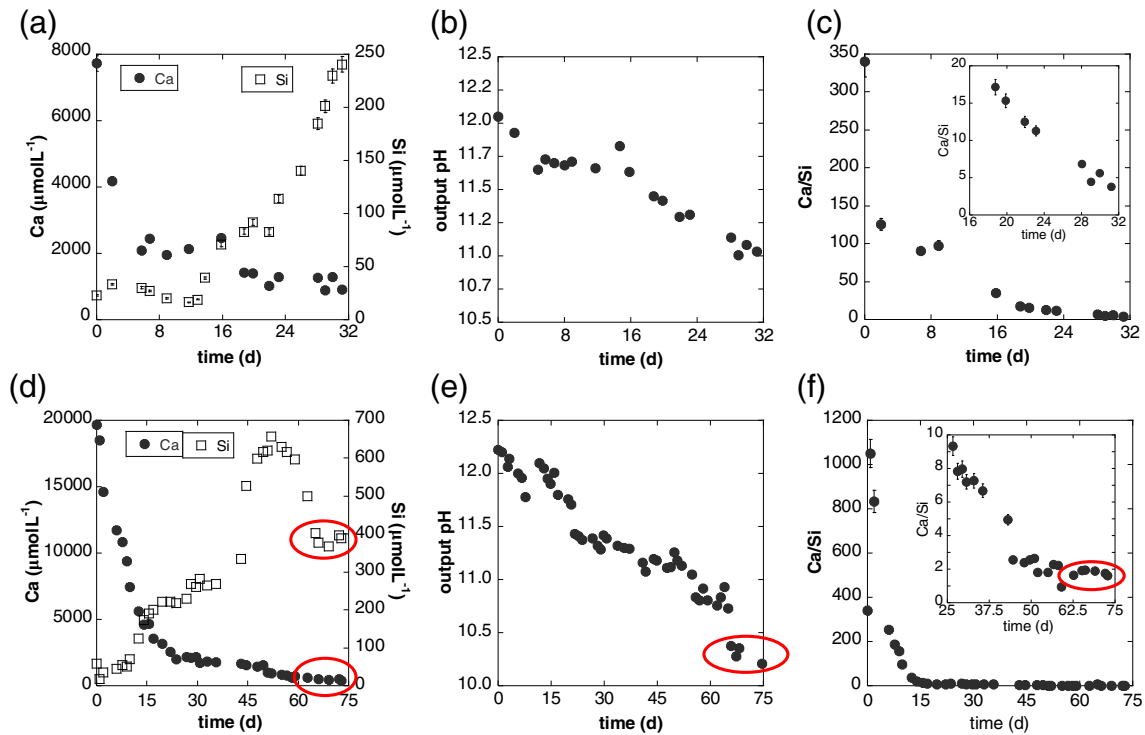


Fig. 2. Two representative experiments: top (experiment C–S–H–5): steady state was not approached (see text); variation of output concentration of Ca and Si (a), output pH (b) and aqueous Ca/Si ratio (c) with time. Bottom (experiment C–S–H–8): steady state was approached (see text); variation of output concentration of Ca and Si (d), output pH (e) and aqueous Ca/Si ratio (f) with time. Ellipses indicate steady state. Uncertainties associated to measure concentrations and Ca/Si ratios are 3% and 10%, respectively. The insets in (c) and (f) show the variation of the aqueous Ca/Si ratio with time in the last 17 and 30 days, respectively. For more details see Trapote-Barreira et al. [15].

amounts of wet powder samples were placed into 1 mm quartz optical cells to prevent sample drying during the measurements. The wet powders were allowed to settle for 2 h before the SANS experiments.

3. Results and discussion

3.1. C–S–H gel dissolution

The flow-through experiments were performed with different durations (from 16 days to 74 days) to evaluate changes in the liquid and solid composition with time. Therefore, steady-state conditions were only reached in the longest experiments (Fig. 2a,b,d,e). The observed decrease in output Ca concentration and decrease in output pH with time, together with the increase in Si, indicate that portlandite and C–S–H gradually dissolved. The decrease in the aqueous Ca/Si ratio indicates that the high Ca concentration at the start of the experiments was mainly due to an initial dissolution of portlandite (Fig. 2c and f). As portlandite was mostly dissolved, the C–S–H gel dissolution was incongruent, showing preferential Ca release and consequent gradual decrease in the aqueous Ca/Si ratio (Table 2). In the longest experiments, C–S–H gel dissolution reached steady state, i.e., the output Ca and Si concentrations were constant with time (Fig. 2d,e), and the Ca and Si output concentrations were similar within the measurement uncertainties, yielding aqueous Ca/Si ratio of 1.0 ± 0.1 (congruent dissolution) (Fig. 2c,f). The results agree with those reported by Harris et al. [3] and Carey et al. [25,26] who showed that the leaching of C–S–H gels in demineralized water could initially be described as an incongruent dissolution, tending gradually to a congruent dissolution. Overall, the observed behavior suggests that after ≈ 70 days, the reacted samples merely consisted of C–S–H powder grain particles. This fact was corroborated by XRD analyses (Fig. A2), which showed the samples to be only composed of C–S–H, as no peaks of portlandite were observed, indicating thus that portlandite was mostly exhausted. Moreover, the composition of the remaining C–S–H powder grain particles showed a

solid Ca/Si ratio of 1.03 ± 0.10 (1σ), which is close to that of a tobermorite-like phase (molar Ca/Si = 0.83) (Fig. 2f). BET measurements showed significant variation in reactive area during C–S–H gel dissolution, which has implications in the quantification of the C–S–H dissolution kinetics [15]. As the Ca/Si ratio decreased to a value close to a tobermorite stoichiometric value of 0.83, the C–S–H dissolution rate, based on the Si release (R_{Si}), increased from $4.50 \times 10^{-14} \text{ mol m}^{-2} \text{ s}^{-1}$ ($\log R_{Si} = -13.3$) to $6.69 \times 10^{-12} \text{ mol m}^{-2} \text{ s}^{-1}$ ($\log R_{Si} = -11.2$; Table 2). Fig. 3 depicts the variation of $\log R_{Si}$ as a function of the Ca/Si aqueous ratio. It is observed that as the aqueous Ca/Si ratio diminishes to around 60 (i.e., dissolution of portlandite is mainly taking place), the dissolution

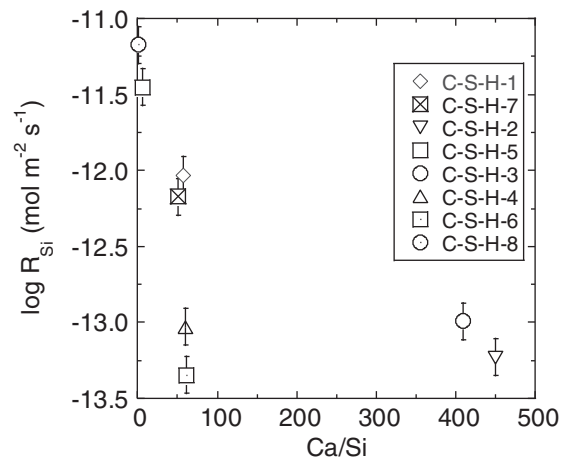


Fig. 3. Logarithm of the final state dissolution rates (R_{Si}) versus aqueous Ca/Si ratio (see results presented in Table 2). Vertical bars represent statistical standard deviation uncertainties (1σ). As the aqueous Ca/Si ratio diminishes from around 450 to around 60 (i.e., dissolution of portlandite is mainly taking place), the dissolution rates are the same within the estimated uncertainty of 15%. And the rates increased as long as the C–S–H gel was the main dissolving phase.

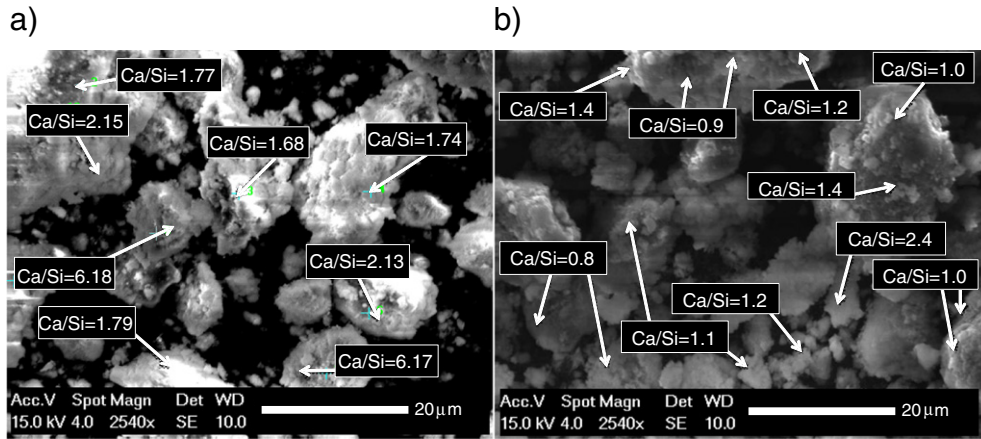


Fig. 4. SEM images showing (a) hydrated C₃S particles rich in C–S–H gel and Ca(OH)₂ in the initial (unreacted) sample. The microprobe analysis shows that the Ca/Si ratio of the C–S–H regions is 1.74 ± 0.10 ; a Ca/Si ratio higher than 2.5 indicates the presence of portlandite; (b) after 73 days of reaction most of the cement particles shown are of modified C–S–H composition with a Ca/Si ratio of 1.02 ± 0.09 .

rates are the same within the estimated uncertainty of 15%. And the rates increased as long as the C–S–H gel was the main dissolving phase, which implies a change from the initial C–S–H structure to that of a tobermorite-like phase.

Comparison of SEM images and EDX analyses between the unreacted (hydrated sample prior to dissolution) and the reacted samples (hydrated sample after flow-through dissolution) shows that most of the portlandite dissolved during the experiments (Fig. 4).

3.2. ²⁹Si-NMR: C–S–H gel and portlandite

In the ²⁹Si MAS-NMR spectra (Fig. 5), the tetrahedral coordination is expressed by means of Q¹, Q^{1p}, Q², Q^{2v}, Q²ⁱ, Q^{2p} and Q³-defect, denoting the chemical shift (ppm) of a silicon atom bonded to n bridging

oxygens. Q¹ and Q^{1p} denote a chain-end tetrahedron, Q² is a chain-intermediate tetrahedron (silicate tetrahedra coordinated to the calcium ions), Q^{2p} denotes a bridge tetrahedron bonded to two protons, Q²ⁱ is a bridge tetrahedron bonded to a proton and a calcium ion, Q³-defect is a tetrahedron surrounded by three silica tetrahedra where two are Q² and the third is another Q³-defect (linking two silicate chains in the interlayer space). A Q² tetrahedron linked to a Q³-defect is a Q^{2v}. The deduced values of Q²/Q¹ ratio indicated that the solid C–S–H polymerization [15], i.e., the linear silicate chain length, increased with time (Q¹ intensity decreases and Q² intensity increases resulting in Q²/Q¹ ratio increase; Fig. 5). Likewise, Fig. 6a shows that the Q²/Q¹ ratio increased as a function of the aqueous Ca/Si ratio. Fig. 6b shows pH and Q²/Q¹ ratio as a function of time multiplied by flow rate and divided by sample mass pH. Altogether indicates that as pH decreased to a constant value

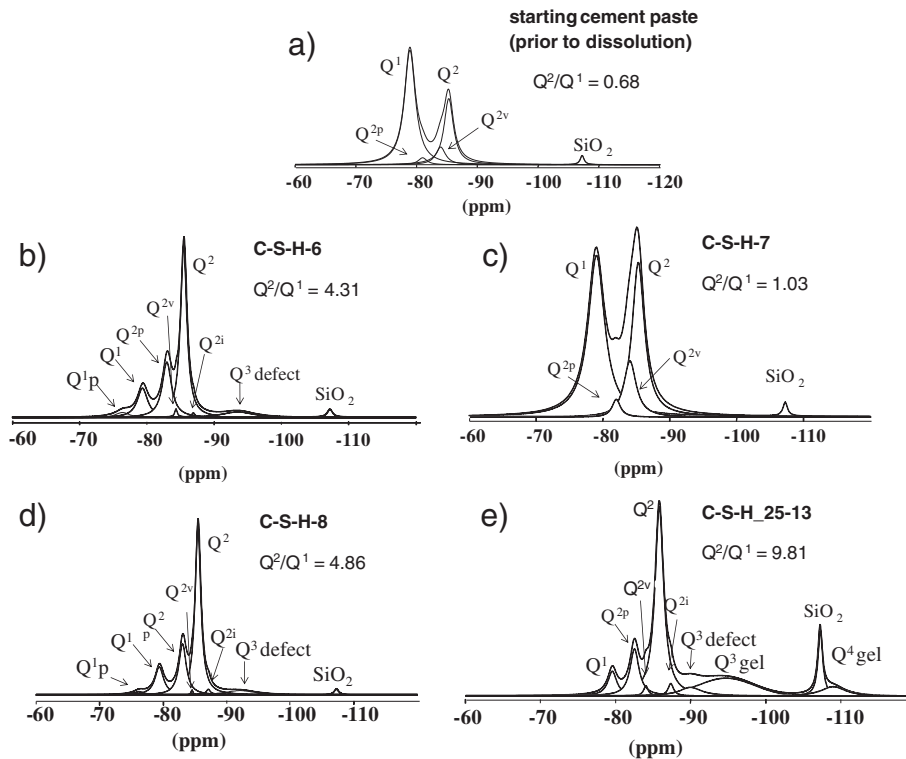


Fig. 5. Deconvolution of the ²⁹Si MAS-NMR spectra of the hydrated C₃S sample prior to dissolution (a) and the reacted samples in experiments C–S–H-6 (b), C–S–H-7 (c), C–S–H-8 (d) and C–S–H-25–13 (e) that underwent different degrees of dissolution; Q₂/Q₁ ratios indicate the evolution of the solid C–S–H polymerization. An extended explanation of the results is given by Trapote-Barreira et al. [15].

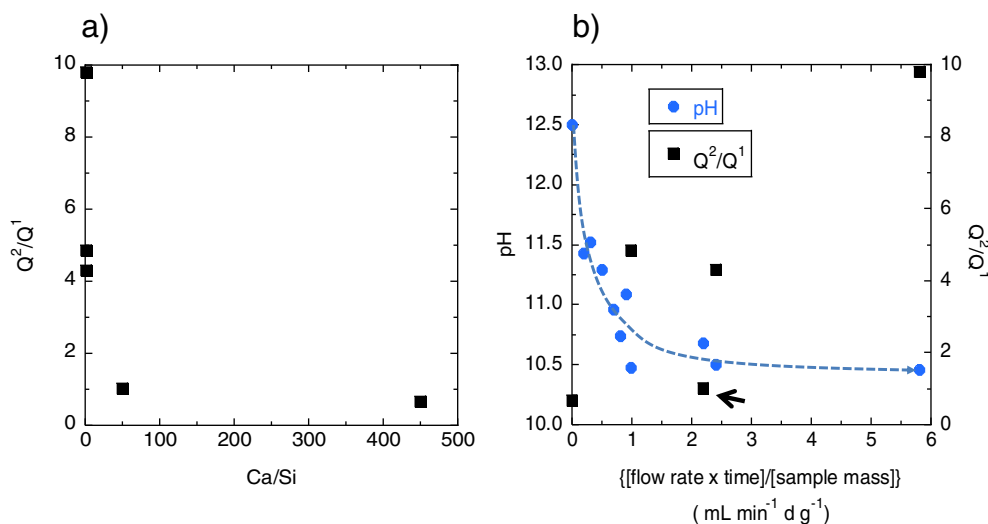


Fig. 6. Variation of (a) Q^2/Q^1 ratio as a function of aqueous Ca/Si ratio and (b) output pH and Q^2/Q^1 ratio as a function of flow rate \times time/sample mass. Arrow indicates an outlier value of Q^2/Q^1 ratio (see text). The values of Q^2/Q^1 ratio were calculated according to [15]. Dotted line indicates tendency.

(ca. 10.50), the Q^2/Q^1 ratio (C–S–H gel polymerization) tended to increase with dissolution. This is evidence that the partial dissolution of solid C–S–H leaves a residual structure that may be similar to a more ordered tobermorite structure. The attainment of similar aqueous and solid Ca/Si ratio values, respectively ($\text{Ca/Si}_{\text{aqueous}} = 1.20 \pm 0.15$ (1σ)) and $\text{Ca/Si}_{\text{solid}} = 1.03 \pm 0.16$ (1σ), close to that of tobermorite ($\text{Ca/Si}_{\text{solid}} = 0.83$) strongly supports this trend (Table 2, Fig. 4). This fact implies both a gradual change in solid C–S–H composition accompanied by a gradual change from non-stoichiometric C–S–H dissolution to stoichiometric dissolution.

3.3. SANS

3.3.1. Neutron scattering contrast: initial C–S–H gel

It is necessary to determine the scattering contrast from the composition and density of the C–S–H gel to calculate the SANS surface area. As both, the composition and density of the gel, are a priori unknown and needed to calculate the neutron scattering length density ($\rho_{\text{C–S–H}}$), the relative scattering contrast of the starting C–S–H was

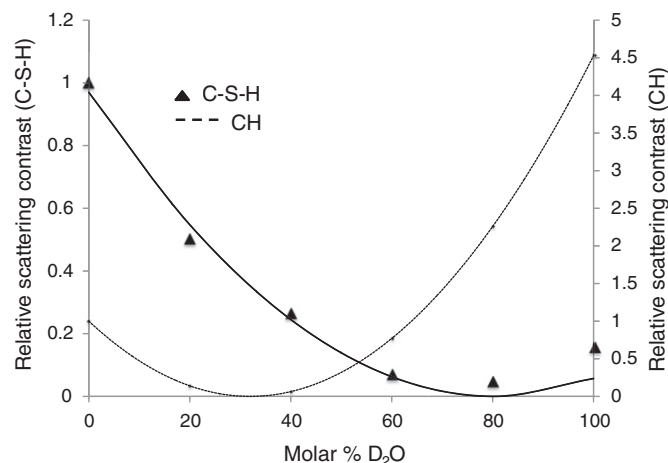


Fig. 7. Relative SANS intensity (scattering contrast) data versus molar D_2O content (triangles, with experimental uncertainties smaller than the size of the symbols), together with the two-component parabola fit for the initial C–S–H gel sample (line) and calculated scattering curve of pure portlandite, $\text{Ca}(\text{OH})_2$, (CH) (dashed line).

obtained from calculation of the Porod constants, which were normalized to that obtained at 100% H_2O (contrast variation method) (Fig. 7). Using six specimens with varying the $\text{H}_2\text{O}/\text{D}_2\text{O}$ fluid mixture the Porod constants were calculated from the linear fit of lq^4 vs. q^4 according to Eq. (3) in the Porod regime data ($0.11 \text{ \AA}^{-1} < q < 0.2 \text{ \AA}^{-1}$), where the scattering is dominated by the nanoscale C–S–H gel–water interface [13] (Table 3).

In a system with $\text{H}_2\text{O}/\text{D}_2\text{O}$ fluid and solid C–S–H, the scattering intensity drops to zero at the contrast matchpoint. This occurs when the solid scattering-length density ($\rho_{\text{C–S–H/D}}$) of C–S–H where the H content has partially exchanged for D content and the pore fluid density (ρ_{liquid}) with an identical $\text{H}_2\text{O}/\text{D}_2\text{O}$ mix as in the C–S–H/D solid are the same, resulting in a nil scattering contrast. However, in a system with $\text{H}_2\text{O}/\text{D}_2\text{O}$, solid C–S–H/D and CH when $\rho_{\text{liquid}} = \rho_{\text{C–S–H/D}}$, the experimentally measured contrast never goes to zero because scattering contributions from nanoscale CH become non-negligible [27]. Fig. 7 shows the C–S–H gel non-zero contrast minimum, which indicates the presence of both solid C–S–H and fine CH crystals as expected from the initial composition of C–S–H gel ($\approx 67\%$ mass solid C–S–H and $\approx 27.5\%$ mass CH).

When scattering contributions at high- Q are from two solid phases (C–S–H and CH), the measured contrast curve can be fitted with two-component parabolas, yielding a single parabola with a minimum value greater than zero. The first parabola accounts for CH with a 31% (molar) D_2O matchpoint and the second one for C–S–H gel constrained only by requiring zero intensity at contrast match [8]. The two fitting

Table 4
Calculated neutron scattering length density and contrast values for the CH.

Molar % D_2O	Neutron scattering length density $\text{H}_2\text{O}/\text{D}_2\text{O}$ ($\times 10^{14} \text{ m}^{-2}$)	Neutron scattering contrast factor between CH and pore fluid ($\times 10^{28} \text{ m}^{-4}$)	Relative scattering contrast factor between CH and pore fluid
0	−0.561	4.837	1
20	0.816	0.677	0.140
31	1.573	0.044	0
40	2.192	0.305	0.063
60	3.568	3.719	0.769
80	4.944	10.92	2.258
100	6.320	21.91	4.529

Neutron scattering length density of $\text{Ca}(\text{OH})_2$ (CH in cement chemistry notation) is equal to $1.64 \cdot 10^{14} \text{ m}^{-2}$ [8].

Table 5
Composition and density of the C–S–H gel according to the literature values.

Bulk formula	Density	Contrast MP (molar % D ₂ O)	Scattering contrast factors {in D ₂ O/in H ₂ O}	Reference
	(g cm ⁻³)			
C ₃ S ₂ H _{2.5}	2.15	58.3	0.513	[27,28]
C _{1.67} SH	2.10	76.2	0.115	[32]
C _{1.5} SH _{2.5}	2.15	72.7	0.141	[25]
C _{1.7} SH ₄	1.90	57.7	0.600	[25]
C _{1.7} SH _{2.1}	2.18	66.2	0.260	[25]
C _{1.7} SH _{1.8}	2.604	81.0	0.045	[13]

The values of bulk formula and density used in this study are from [13].

parameters are (1) the small fractional intensity contribution from nanoscale CH (f_{CH}), which is subtracted from the known neutron scattering length density of CH, and (2) the contrast matchpoint of the C–S–H gel. The C–S–H gel mass density, the H/D ratio (from the H₂O/D₂O exchange), and the C–S–H gel composition are obtained from [13]. The calculated contrast curve for CH ($\rho_{CH} = 1.643 \times 10^{14} \text{ m}^{-2}$) is shown in Fig. 7 and the computed scattering contrast data is listed in Table 4.

The solid C–S–H/D contrast matchpoint with H₂O/D₂O fluid takes place with 81% D₂O (Fig. 7). This value was obtained by subtracting the intensity contribution from nanoscale CH ($f_{CH} = 1.66\%$). To determine the correct C–S–H/H₂O scattering contrast, the measured relative scattering contrast data were fitted using different values of C–S–H gel chemical composition and density published in previous C–S–H gel hydration studies (Table 5). Early studies [28,29] using the C₃S₂H_{2.5} composition and density of 2.15 g cm³ obtained a reasonable match between the experimental contrast data and the predicted curve. Thomas et al. [27] obtained experimental contrast data and relative scattering contrast as a function of D₂O content, using four theoretical C–S–H gel formula (the previous one by Allen et al. [28] and three new ones which were derived under three different conditions: D-dried, water-saturated and equilibrated to 11% RH). The best match was obtained with the latter one (C_{1.7}SH_{2.1}) and density of 2.18 g cm³. Recently, Allen et al. [13] suggested a new C–S–H

composition and density (C_{1.7}SH_{1.8} and 2.604 g cm³) to be more precise as it was able to distinguish water within the C–S–H nanostructure, which includes water physically bound within the internal structure of the nanoparticles.

An evaluation of the quality of the fit curves of the experimental data was made following Thomas et al. [27]. Best fit parabola was obtained using the C–S–H gel chemical composition and density of C_{1.7}SH_{1.8} and 2.604 g cm⁻³ reported by Allen et al. [13] and is shown in Fig. 7. For a H₂O saturated C–S–H gel specimen, the neutron scattering length density (ρ_{C-S-H}) and the neutron scattering contrast ($\Delta\rho^2$) are calculated as

$$|\Delta\rho|^2 = (\rho_{C-S-H} - \rho_{H_2O})^2 \tag{4}$$

where ρ_{H_2O} is the neutron scattering length density of water. ρ_{C-S-H} and $\Delta\rho^2$ values were $2.572 \times 10^{14} \text{ m}^{-2}$ and $9.83 \times 10^{28} \text{ m}^{-4}$, respectively. Nonetheless, in the calculations the slightly modified $\Delta\rho^2$ value of $9.64 \times 10^{28} \text{ m}^{-4}$ was used because it takes into account the presence of scattering from nanoscale CH at high q [13].

Once C–S–H composition, density and the scattering contrast were known, SANS measurement for initial and leached C–S–H samples were performed at 31% D₂O (CH match), and changes in the structure of the C–S–H could be quantified over a scale range from 10 Å to 10⁴ Å [13].

3.3.2. SANS data: reacted C–S–H gel

Fig. 8 shows the SANS data obtained in H₂O/D₂O fluid mixture of 31% ($0.001 < q \text{ (Å}^{-1}\text{)} < 0.22$) for the starting (unreacted) C–S–H gel and reacted C–S–H gel samples in a log–log plot of $I(q)$ versus q . Under these circumstances, the scattering contrast between CH and the pore fluid is matched out, and the scattering contrast is almost entirely that between solid C–S–H/D (with 31% of the C–S–H bound H exchanged for D) and H₂O/D₂O with 31% D₂O. Changes with time in the shape of the SANS data in this plot suggest that microstructural changes occurred in the reacted samples. SANS is particularly useful for measuring the surface area of cement paste because it is noninvasive and is performed on saturated specimens [27]. For cement based materials, the surface area is dominated by that between the C–S–H gel and the pore H₂O

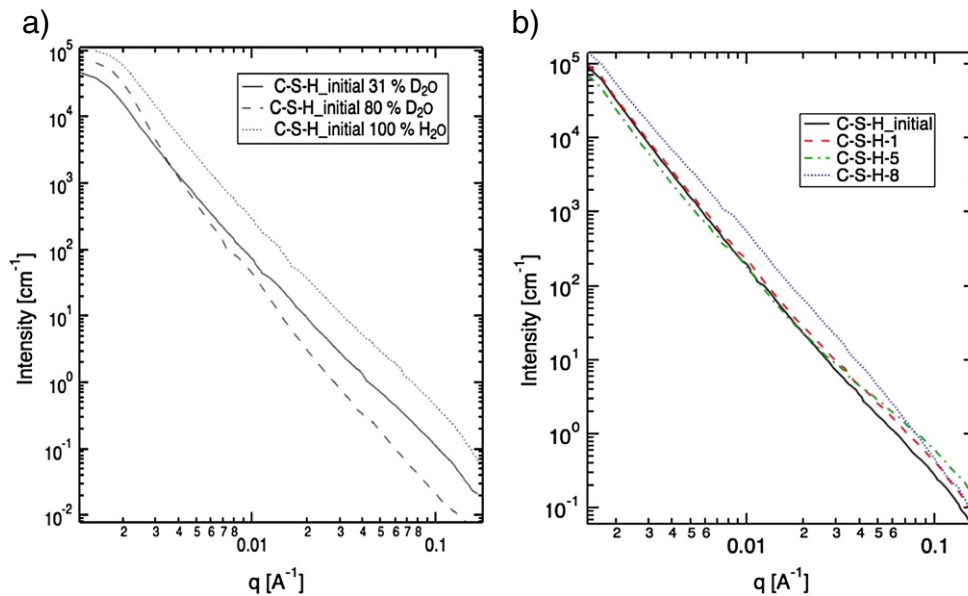


Fig. 8. SANS data for the initial (unreacted) C–S–H gel sample (a) and reacted C–S–H gel samples (b) in log–log plots of $I(q)$ versus q . Data scatter representative of the standard deviation uncertainties (1σ). In a) the SANS data given for the hydrated paste (prior to dissolution) mixed with 100% H₂O solution, 31% and 80% D₂O solutions illustrate that in 31% D₂O solution the intensity is given by the C–S–H gel (same slope as that in 100% H₂O solution) and in 80% D₂O solution the intensity is given by CH (i.e., MP of C–S–H gel). In b) the SANS data for the C–S–H gel samples rescaled to their predicted contrast in H₂O.

Table 6

Porod constant (C_p), Porod surface area (S_T), calculated total internal surface area (SSA) and specific surface area (BET) of the reacted C–S–H gel samples.

Experiment	Time (day)	C_p ($\times 10^{-12} \text{ \AA}^{-5}$)	S_T ($\text{m}^2 \text{ cm}^{-3}$)	SSA ($\text{m}^2 \text{ g}^{-1}$)	BET
C–S–H_initial	0	0.49 ± 0.01	78.96 ± 1.70	30.32 ± 0.57	11.7
C–S–H-1	16	0.88 ± 0.08	126.1 ± 11.6	48.41 ± 4.47	14.5
C–S–H-2	16	0.68 ± 0.07	97.38 ± 10.7	37.39 ± 4.14	52.7
C–S–H-3	16	0.71 ± 0.08	101.5 ± 12.7	38.99 ± 4.88	18.6
C–S–H-4	17	0.59 ± 0.06	84.33 ± 9.38	32.38 ± 3.60	25.0
C–S–H-5	31	1.16 ± 0.07	150.2 ± 10.2	57.67 ± 3.91	46.1
C–S–H-6	44	1.01 ± 0.07	130.9 ± 9.10	50.26 ± 3.49	61.6
C–S–H-7	67	0.79 ± 0.07	98.66 ± 9.16	37.88 ± 3.51	15.9
C–S–H-8	74	0.70 ± 0.08	87.60 ± 9.22	33.64 ± 3.75	42.9

Estimated standard deviation measurement uncertainty is 10% for BET (1σ).

[13], and with the CH matched out, the SANS Porod surface area should be entirely that between C–S–H and the H_2O pore fluid. In a two-phase specimen, the specific surface area per unit specimen volume (S_T), between the two phases as determined from small angle scattering can be written as [28]:

$$S_T = \frac{C_p}{2\pi|\Delta\rho|^2} \quad (5)$$

where $\Delta\rho^2$ is the scattering contrast, and the Porod constant (C_p) for the reacted samples was obtained from the linear fits of Iq^4 vs. q^4 with the lowest q value (0.15 \AA^{-1} – 0.2 \AA^{-1}) at the lowest χ^2 [6]. A calculated specific surface area (SSA in $\text{m}^2 \text{ g}^{-1}$) is computed by dividing S_T by the solid C–S–H density (2.604 g cm^{-3}).

Table 6 lists the obtained values of C_p , S_T , SSA and the measured BET specific surface areas of the unreacted and reacted C–S–H gel samples, using the composition and density (2.604 g cm^{-3}) obtained by Allen et al. [13]. The derived S_T for the initial C–S–H gel sample is lower than (178 ± 4.8) $\text{m}^2 \text{ cm}^{-3}$, which was obtained by Thomas et al. [6] with a density of 1.457 g cm^{-3} . Fig. 9a depicts the variation of S_T , S_{SF} and S_{VF} with reacting time multiplied by flow rate and divided by sample mass. S_T increases significantly from (78.96 ± 1.70) $\text{m}^2 \text{ cm}^{-3}$ to (150.2 ± 10.2) $\text{m}^2 \text{ cm}^{-3}$ after $0.86 \text{ mL min}^{-1} \text{ d g}^{-1}$ (31 days), thereafter decreasing to (87.60 ± 9.22) $\text{m}^2 \text{ cm}^{-3}$ as dissolution continues. This behavior is consistent with that shown by Thomas et al. [7] in which the total internal surface area of leached OPC first increased from $120 \text{ m}^2 \text{ cm}^{-3}$ to $200 \text{ m}^2 \text{ cm}^{-3}$ as the Ca/Si ratio

decreased to 1, with the surface area thereafter decreasing as the Ca/Si ratio decreased below 1, due to thickening of the (now sheet-like) fundamental C–S–H units. S_{VF} shows a similar tendency to that of S_T . The significant stochastic variation and a rather large S_{SF} suggest that the powdered nature of the samples may affect the obtained values in comparison to the values calculated from monolithic hydrated cement coupons used in previous studies [7,13].

A working assumption is that the density for the unreacted and reacted C–S–H gel is constant (2.604 g cm^{-3}) (similar to that of tobermorite and jennite), the specific surface area (SSA) is calculated from the S_T values. The resulting SSA ranged from (30.32 ± 0.57) $\text{m}^2 \text{ g}^{-1}$ (initial C–S–H) to (57.67 ± 3.91) $\text{m}^2 \text{ g}^{-1}$ in the reacted C–S–H (Table 6, Fig. 9b). The C–S–H gel is often conceived by simplification to be formed by two components, a high-density (HD) inner-product and a low-density (LD) outer-product [30]. It is considered that the former product is a rough and dense disordered particulate matrix, and the latter is a lower dense phase and SANS sensitive. The LD C–S–H gel is the component of the microstructure that remarkably contributes to the measured BET specific surface area [31]. Fig. 9b depicts the measured BET specific surface area variation with time and compares with the SSA variation. On the one hand, in terms of magnitude, the SSA and BET are fairly comparable, even though lower BET values could be systematically expected since nitrogen physisorption may not access the interlayer C–S–H porosity. It is found that SANS-based surface areas are remarkably consistent [13], providing the right criteria are used to extract the Porod constant. It is observed that the BET values tend to increase with time up to ≈ 40 days and decrease thereafter. This behavior that is similar to that of S_T could be caused by the increase of the LD products as the HD C–S–H gel dissolves. This increase in LD products yields large accessible area to nitrogen physisorption and neutron scattering. However, as more material is leached or dissolved away over longer times, the surface area declines. The trend of SSA and BET surface areas could correspond to a change in the fundamental C–S–H gel units that evolve into a sheet-like morphology [7].

3.3.3. Volume-fractal and surface-fractal structure

The obtained SANS intensity data for the starting C–S–H gel and reacted C–S–H samples were rescaled to the predicted contrast in H_2O . The scattering contrast value for the unreacted C–S–H sample was $9.64 \times 10^{28} \text{ m}^{-4}$ (see Section 3.3.1) and for the reacted C–S–H samples were those obtained by Thomas et al. [7]. Fig. 10a and b shows the SANS data for the hydrated sample prior to dissolution and a hydrated

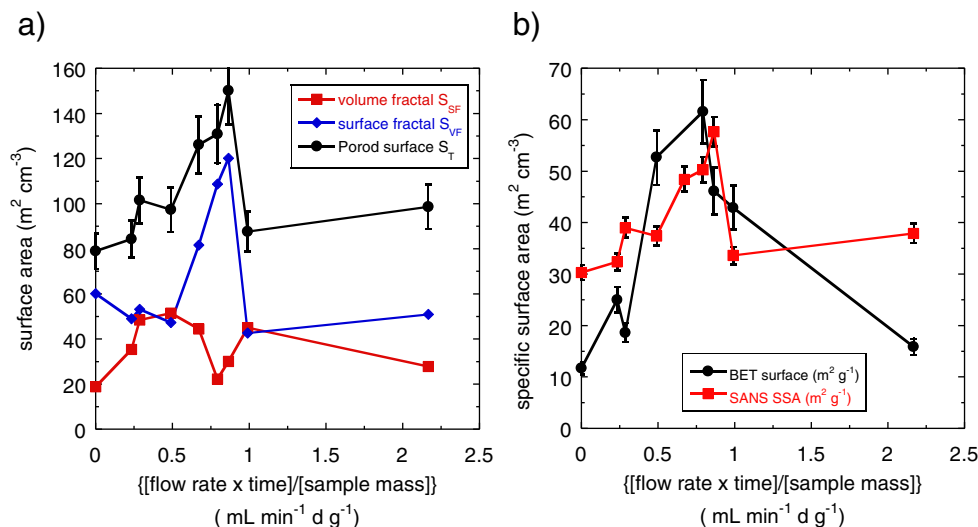


Fig. 9. Variation of surface area as a function of flow rate \times time/sample mass: a) total surface area (S_T), surface fractal (S_{SF}) and volume fractal (S_{VF}) and b) calculated specific surface area (SSA) and measured BET specific surface area. Vertical bars represent standard deviations.

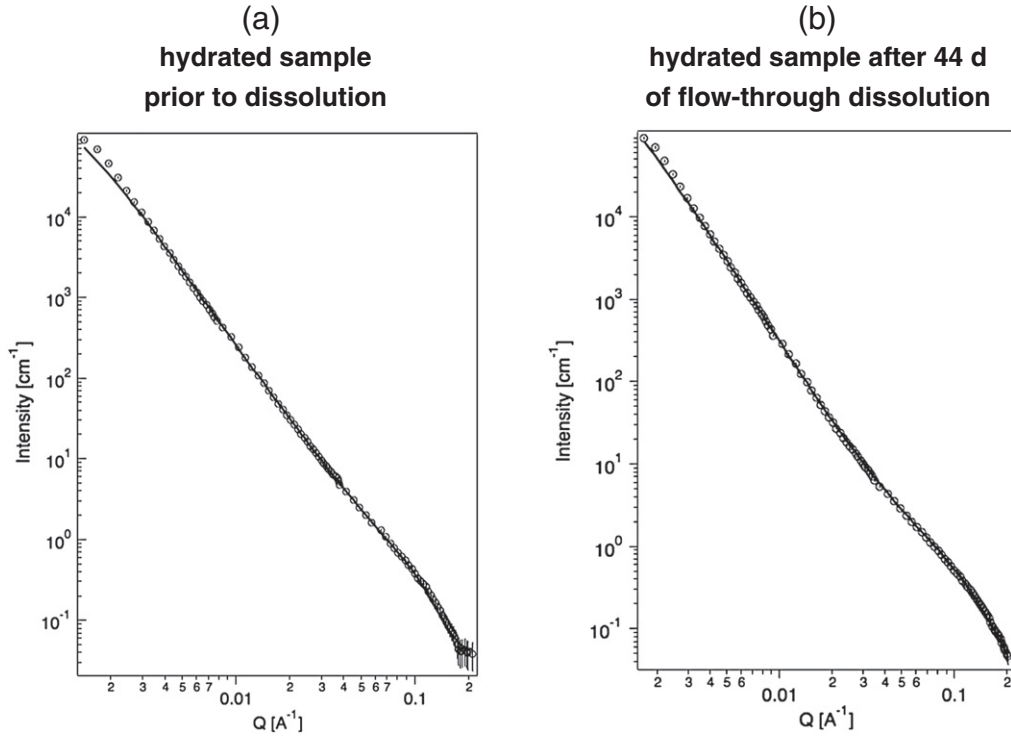


Fig. 10. Small-angle neutron scattering data (solid lines) and fits using the fractal model (Eq. (A1)) (open circles) for hydrated sample prior to dissolution (left) and hydrated sample after 44 days of flow-through dissolution (experiment C–S–H-6) (right). There is an excellent agreement between the experimental and fractal model data.

sample after 44 days of flow-through dissolution in a log–log plot of $I(q)^4$ vs. q with fit background scattering removed, respectively. The neutron scattering contrast used was $9.64 \times 10^{-28} \text{ m}^{-4}$. According to the fractal model [13], the scattering cross-section is separated into three component terms: volume fractal, surface fractal and Porod regime (Eq. (A1)). The surface fractal regime occurs at the q range from 0.002 \AA^{-1} to about 0.02 \AA^{-1} , and the volume-fractal regime ranges from $\approx 0.02 \text{ \AA}^{-1}$ to $\approx 0.1 \text{ \AA}^{-1}$. Primarily, surface-fractal and volume-fractal model

components were used separately to fit the data in these q -ranges to guarantee a physical significance of the components. Fractal model, based on the Colloidal Model-I [32], considers that the building blocks are globules with a $\approx 5 \text{ nm}$ in diameter filled of basic units of 2.2 nm . Thus, with a reasonable fit, all parameters were varied together assuming prolate gel globules with an aspect ratio of $\beta = 2$ and then assuming oblate gel globules ($\beta = 0.5$). Doing each fit twice in this way tests the stability of the fit at high Q , and it also greatly reduces the strong Bessel

Table 7

Fit and derived microstructure parameters from the fractal model. Estimated uncertainties (standard deviation) for each value are given in parentheses. Fixed ξ_s values from 700 to 9000 \AA yield S_0 uncertainties lower than 10%.

Parameter (local packing parameter η set to 0.5)	C–S–H_initial	C–S–H-1	C–S–H-2	C–S–H-3	C–S–H-4	C–S–H-5	C–S–H-6	C–S–H-7	C–S–H-8
Duration (day)	0	16	16	16	17	31	44	67	84
$D_o = R_c (\text{\AA}) = 2R_c^f$	47.37 (2.15)	43.37 (3.74)	41.89 (0.85)	44.26 (3.33)	45.21 (8.02)	35.08 (3.92)	33.25 (18.29)	41.43 (23.24)	72.72 (4.09)
$\phi_{C-S-H} (\%)^f$	4.093 (0.289)	4.025 (1.245)	5.757 (0.759)	6.022 (0.802)	4.930 (1.404)	5.855 (1.107)	2.887 (0.737)	2.007 (2.409)	3.184 (0.866)
D_V^f	2.369 (0.078)	2.132 (0.335)	2.045 (0.129)	2.244 (0.109)	1.955 (0.154)	1.907 (0.158)	1.538 (0.178)	1.821 (0.927)	2.038 (0.305)
$\xi_V (\text{\AA})^f$	176 (52)	60 (25)	78 (26)	198 (73)	189 (130)	44 (10)	54 (65)	40 (46)	124 (111)
$S_0 (\text{m}^2 \text{cm}^{-3})^f$	0.412 (0.005)	0.471 (0.038)	0.676 (0.049)	0.711 (0.033)	0.671 (0.024)	2.011 (0.159)	2.163 (0.049)	5.725 (0.0752)	6.806 (0.906)
D_S^f	2.729 (0.011)	2.844 (0.022)	2.813 (0.027)	2.794 (0.021)	2.749 (0.076)	2.807 (0.018)	2.611 (0.019)	2.559 (0.008)	2.7878 (0.013)
$\xi_S (\text{\AA})$	9000	9500	8800	9000	9000	1000	1500	700	800
Total S_T ($\text{m}^2 \text{cm}^{-3}$) (measured by Porod law)	78.96 (1.70)	126.1 (11.6)	97.38 (10.7)	101.5 (12.7)	84.33 (9.38)	150.2 (10.2)	130.9 (9.10)	98.66 (9.16)	87.60 (9.22)
$S_{SF} (\text{m}^2 \text{cm}^{-3})^d$	18.88	44.51	52.24	48.37	35.37	30.03	22.17	27.80	45.01
$S_{VF} (\text{m}^2 \text{cm}^{-3})^d$	60.07	81.56	47.25	53.18	48.96	120.16	108.72	50.90	42.59
$\phi_{MAX} (\%)^d$	9.37	5.27	10.43	18.71	21.97	4.60	5.94	1.94	5.31
$\phi_{MAX}/\phi_{C-S-H} (\%)^d$	2.30	1.31	1.81	3.11	4.46	1.30	2.06	0.97	1.67

f and d denote fitted and derived, respectively.

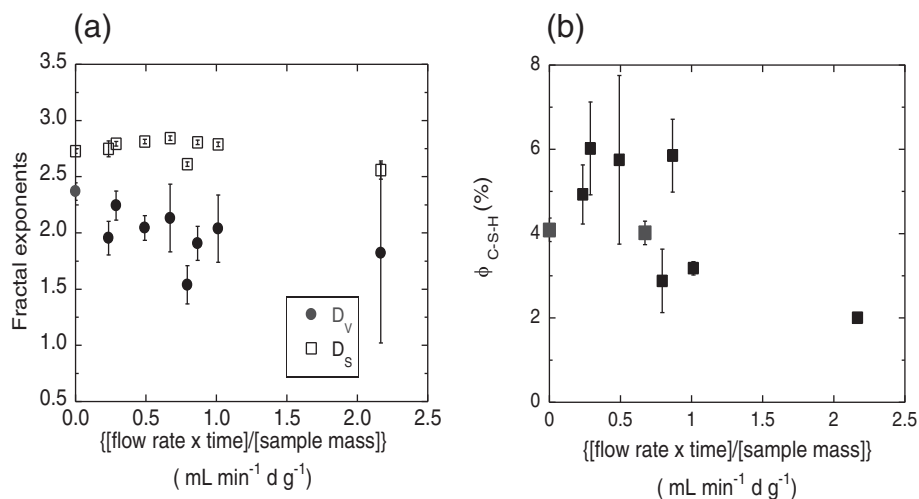


Fig. 11. SANS scattering data: fit fractal parameters as a function of time. Vertical bars, where visible, represent the estimated standard deviation uncertainties in the fit results (1σ). a) Variation of fractal exponents with dissolution expressed as a function of flow rate \times time/mass and b) variation of outer C–S–H volume fraction with dissolution expressed as a function of flow rate \times time/sample mass.

function oscillations that would be in the model function for monodisperse spheres. While assuming a C–S–H gel globular shape, they are neither exact spheres nor monodisperse. Taking the average of slightly prolate and slightly oblate globule shapes better approximates the true situation. The obtained R_0 values are converted to a sphere-equivalent radius and then are averaged [13,33].

There is certainly a covariance between S_0 and ξ_s that does not allow these parameters to be fitted independently to the data. Together they define the absolute intensity of the surface fractal scattering. ξ_s has a value beyond where there is true information content in the scattering data. To obtain a reasonable fit, ξ_s cannot be larger than a value between the mean clinker radius and the mean clinker diameter (as this would imply surface fractal scaling going beyond the dimensions of the substrate upon which it is deposited). The mean size of the clinker grains is $\approx 1.9 \mu\text{m}$ and 90% of the C–S–H gel sample has a size $< 8 \mu\text{m}$. The detected S_0 – ξ_s covariance does not affect the overall rough surface-fractal surface area (S_{SF}). Best fits were obtained with the ξ_s value ranging from 700 Å to 9000 Å (Table 7). The best fractal model fits suggest changes in the microstructure of the reacted C–S–H gel during dissolution. This is also inferred from the variation of the fit parameters (Table 7).

The fitted values obtained in the volume or mass-fractal component are the volume fraction of solid C–S–H ($\phi_{\text{C-S-H}}$), the volume or mass

fractal dimension (D_V), the volume or mass fractal correlation length (ξ_V), and the mean radius of the volume fractal building block, R_0 . Two additional terms, the local volume fraction (η) and the correlation hole radius (R_c), are sensitive to the nearest and next nearest neighbor globules and are necessary to create an acceptable fit where the volume fractal transitions at high q to single C–S–H particle scattering.

From the surface fractal component the surface fractal dimension (D_S), which varies from 2 to 3 for non-smooth surfaces, the surface fractal correlation length (ξ_S) and the smooth surface (S_0) are derived. S_0 shows a monotonic increase with dissolution. Three other parameters of interest are obtained assuming that the C–S–H gel globule nanoparticle diameter ($D_0 = 2R_0 = R_c$) is the building block particle size of the fractal morphology: the upper-limit volume fraction per unit sample volume of the whole volume-fractal morphology (ϕ_{MAX}), the fractally-rough surface area (S_{SF}), and the surface area of the volume-fractal morphology (S_{VF}). They provide the relative amount of solid material within the two fractal morphologies. We note that the variations in S_0 and S_{SF} are likely dominated by the finest grains in the powder samples, since these have the highest surface areas, and are likely to be more affected (in proportion to their volume) by the dissolution process. The stochastic variability in fine powder grain content among the samples may not be sufficient to break the observed monotonic increase in S_0 with dissolution, but the variability in surface

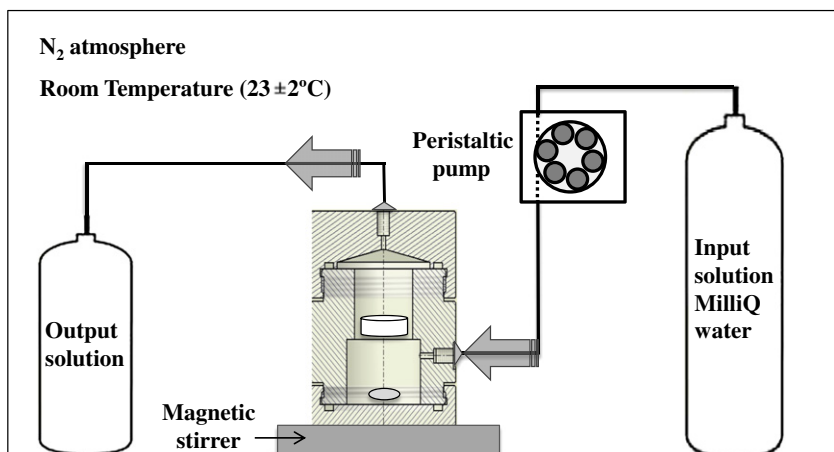


Fig. A1. Schematic representation of the flow-through experiments carried out under CO_2 -free conditions (N_2 atmosphere) inside a glove box.

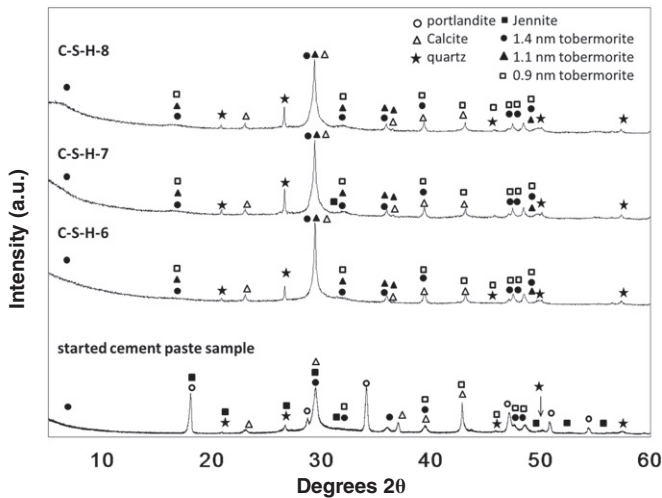


Fig. A2. XRD patterns for the initial C-S-H sample and for reacted C-S-H samples of experiments C-S-H_6, C-S-H_7 and C-S-H_8.

fractal created by different amounts of fine grain material may be sufficient to produce a stochastic S_{SF} , assuming that stochastic variations are amplified in S_{SF} , compared to S_0 .

For the initial C-S-H gel sample, the radius of the building block particles (D_0) obtained is 47.37 Å, and the D_V and D_S values are 2.369 and 2.729, respectively (Table 7). The resulting initial diameter, D_0 , is consistent with previous studies [13]. The D_0 , D_V and D_S values for an unaltered C-S-H gel obtained by [8] were 44.4 Å, 2.61 and 2.55, respectively. Thomas et al. [7] obtained D_V values that range from 2.01 to 2.28 for C-S-H gel in WPC pastes with Ca/Si ratio ranging from 1.47 to 2.4. According to Zarzycki [34] a D_V value of 2.3 is associated with a fractal sphere (C-S-H globules).

In the reacted samples, D_0 tends to slightly decrease from an initial value of 47.37 Å to 35.08 Å after 31 days. Thereafter, it increases to 72.72 Å (Table 7). Such a D_0 increase is consistent with the roughly

equiaxed particles that build the solid C-S-H structure changing their shape with dissolution into sheet-like structures of increasing thickness [7]. D_V tends to slightly decrease for 44 days from 2.369 to 1.538 (Fig. 10a, Table 7) to thereafter increase to 2.038. A decrease in the volume fractal scaling factor suggests that the unreacted C-S-H gel, composed of equiaxed ≈ 5 nm C-S-H gel globule building blocks, transforms to sheet-like structures during dissolution (as the Ca/Si ratio decreases to nearly 1) [36,37], which is in agreement with the results reported by Thomas et al. [7] and Allen et al. [8]. The SANS data together with the ^{29}Si -NMR data (increase in Q^2/Q^1 , longer chain length, and the appearance of Q^3) indicate that the C-S-H gel structure evolves to a more ordered structure, i.e., transformation of the C-S-H gel structure from globule to sheet-like structure. In addition, an increase in D_0 (globule dimension) with Q^2/Q^1 is obtained, but not in a linear fashion as shown by Cappelletto et al. [38]. D_S tends to be constant, merely changing from 2.844 to 2.559 (D_S value of 2 indicates smooth surface) (Fig. 11a), which would indicate an increase in surface roughness during dissolution.

The trend in the volume fraction (ϕ_{C-S-H}) (Fig. 11 b), which essentially is a measure of the amount of LD C-S-H gel (without gel pores) in the paste, is similar to the trend observed for the total internal surface area (S_T). As dissolution progresses, the HD C-S-H gel evolves to LD C-S-H gel, with a maximum after 31 days. Then, LD C-S-H gel continues to dissolve, leading to a volume fraction decrease.

4. Conclusions

The dissolution of the C-S-H gel at room temperature and pH range from 10 to 12.5 has been studied from the aqueous chemistry by means of flow-through reactors and combination of SANS and ^{29}Si -NMR measurements of the evolving solid. This full approach allows us to present the following conclusions.

Regarding the dissolution of the C-S-H gel, it is concluded that the reaction is initially incongruent (i.e., preferential Ca release and consequent gradual decrease in the aqueous Ca/Si ratio) and changes to congruent dissolution of a phase with tobermorite stoichiometry (Ca/Si = 0.83). This behavior is consistent with current C-S-H gel solubility models, e.g. [35]. Likewise, under the experimental conditions of this work, the C-S-H gel dissolution rate increases with decreasing Ca/Si ratio.

SANS data for the unreacted C-S-H gel indicated that the resulting contrast curve was consistent with a solid C-S-H phase with a composition of $C_{1.7}SH_{1.8}$ and density of 2.604 g cm^{-3} as suggested by Allen et al. [13]. SANS data of the evolving C-S-H structure during C-S-H dissolution showed that SANS total internal surface (ST) tends to increase as the Ca/Si ratio decreases to thereafter decrease when the Ca/Si ratio was ≈ 1 . The variation of surface area with time, i.e., when the Ca/Si ratio decreases to reach a tobermorite stoichiometric ratio, is similar for the measured specific surface area (BET) and comparable to the derived SANS surface area (SSA). This observed behavior suggests that, as C-S-H gel dissolves, the morphology of the HD C-S-H gel compound is being transformed to LD C-S-H, increasing the measured specific surface area. Therefore, the use of the BET surface area to normalize the C-S-H gel dissolution rates is fully justified.

The change of the C-S-H gel nanostructure (at the scale range from 10 Å to 1000 Å) during C-S-H gel dissolution was determined from the SANS experimental data fitted with the fractal model [8], considering a fractal structure that is composed of a volume fractal structure, mainly LD C-S-H gel, and a surface fractal structure on the surface of the clinker grains. As dissolution progressed it was inferred that the roughly equiaxed C-S-H gel globules, which comprise the unreacted C-S-H gel structure, change their shape into sheet-like morphology with progressively increasing thickness (D_0 increase). This transformation was supported by the decrease in D_V values (to ≈ 2) which is expected for this structure [7,8]. Surface roughness of the coarse features was inferred by the slight D_S increase. In addition, a decrease in ξ_V and an

Table A1
Parameter definitions for the fractal microstructure model [8] (Eq. (A1)).

Parameters	
ϕ_{C-S-H}	Volume fraction of solid C-S-H gel globules within the entire specimen volume penetrated by the neutron beam. It is essentially a measure of the amount of LD C-S-H (without gel pores) in the paste.
V_p	Volume of a single C-S-H globules. ($V_p = 4\pi\beta R_0^3/3$) where β is the particle aspect ratio.
R_C	Correlation-hole radius. Is the minimum center-to-center distance between C-S-H globules.
R_0	The radius of the building block C-S-H gel globules.
η	Local packing fraction for nearest neighbor C-S-H gel globules.
D_V	Volume fractal scaling exponent. An intensive property of matter that offers a quantitative measure of the volume fractal.
D_S	Surface fractal scaling exponent. An intensive property of matter that offers a quantitative measure of the degree of surface roughness.
ξ_V	Upper-limit length scales (correlation lengths) over which volume fractal scaling apply. Is the maximum size up-to which a volume can be viewed as a fractal.
ξ_S	Upper-limit length scales (correlation lengths) over which surface fractal scaling apply. Is the maximum size up-to which a surface can be viewed as a fractal.
S_0	Smooth geometric surface area on which the surface fractal microstructure is deposited.
$\Gamma(x)$	Mathematical gamma function
$F^2(q)$	Single-particle form factor for C-S-H gel globule
$\Delta\rho^2$	Neutron scattering contrast factor. In this paper, the contrast factors of interest are those between solid C-S-H and H_2O , solid C-S-D and D_2O , solid C-S-H/D and H_2O/D_2O with same given H/D ratios in each, CH and H_2O , CH and D_2O , CH and H_2O/D_2O with any given H/D ratio
BGD	Background intensity.

increase in the $\phi_{\text{MAX}}/\phi_{\text{C-S-H}}$ ratio indicate a loss of structural compaction and density during dissolution.

The C–S–H gel evolution deduced from the SANS experiments is in agreement with the ^{29}Si -NMR measurements that show an increase in polymerization with C–S–H gel dissolution, i.e., dissolution promotes the C–S–H gel structure transformation to a more ordered tobermorite structure.

Acknowledgments

We acknowledge Paul Butler and David Mildner for their scientific support and technical assistance in the SANS measurements at NIST. This work utilized facilities supported in part by the National Science Foundation under Agreement No. DMR-0944772. This study was financially supported by ENRESA (project 0078000174). We also would like to acknowledge two anonymous reviewers for their constructive comments that increased the quality of the paper.

Appendix A

The scheme of the flow-through experiments is show in Fig. A1.

Fig. A2 shows the XRD patterns for the initial and reacted C–S–H gel samples (experiments C–S–H_6, C–S–H_7 and C–S–H_8). The peaks of the diffractograms were assigned to jennite structure (in the initial C–S–H gel) and jennite and tobermorite structures in the reacted samples [39–41]. Nonetheless, it is difficult to determine either the predominant tobermorite (14 Å, 11 Å or 9 Å; Myers et al. [42]) or the existence of jennite because some peaks or bands overlap. However, the presence of the 1.1 nm tobermorite is ruled out in the initial C–S–H gel sample because no Q^3 units were obtained in the ^{29}Si -NMR spectra. Jennite was only considered to be in the initial C–S–H gel sample because its presence is associated to high Ca/Si ratios (e.g., [39–41]),

Fractal model [8].

The full fractal model combines a mass or volume fractal scattering term, attributed to the outer product between grains and a surface-fractal scattering term, and outer product deposited at the clinker grain boundaries and on inert surfaces, such as those of micrometer scale CH crystallites. Nonetheless, the surface fractal may include some inner product formed topochemically. The fractal model fitted the following expression [13,22]:

$$I(q) = \varnothing_{\text{C-S-H}} V_p \Delta \rho^2 \left\{ \frac{\eta R_c^3 \left(\frac{\xi_v}{R_c} \right)^{D_v}}{\beta R_0^3} \times \frac{\sin[(D_v-1)\arctan(q\xi_v)]}{(D_v-1)q\xi_v [1 + (q\xi_v)^2]^{\frac{(D_v-1)}{2}}} \right. \\ \left. + (1-\eta)^2 \right\} F^2(q) + \frac{\pi \xi_s^4 \Delta \rho^2 S_0 \Gamma(5-D_s) \sin[(3-D_s)\arctan(q\xi_s)]}{[1 + (q\xi_s)^2]^{\frac{(5-D_s)}{2}} q \xi_s} + \text{BGD} \quad (\text{A1})$$

where the involved fit parameters are summarized in Table A1. Eq. (A1) consists of three component terms: volume fractal incorporating a single globule ($F^2(q)$) term, surface fractal and flat background scattering.

The first volume-fractal term contains $\phi_{\text{C-S-H}}$, ξ_v , and the mean radius, R_0 , and shape aspect ratio, β , of the building-block C–S–H gel globules in the volume-fractal phase, here assumed to be spheroids. It also contains a local volume fraction, η , and the mean correlation-hole radius, R_c : the mean nearest-neighbor separation of the gel-globule centers.

For C–S–H gel, it is assumed that both the volume-fractal and the surface-fractal morphologies have lower cut-off dimensions of $\approx R_c$, approximately the diameter of one 4–5 nm C–S–H globule: the center of one globule cannot come within R_c of the center of its neighbor without the globules being inside each other.

Within the correlation hole radius, there is a local packing fraction given by η , where $\eta = 1/8$ even in the case of an isolated globule. For a globule linked with two others in a chain, $\eta \approx 1/4$. The maximum η value would be ≈ 0.74 assuming all globules were spheres and having an ordered close-pack. For random close packing $\eta \approx 0.634$; in general, η ranges from 0.5 to 0.65.

The volume-fractal regime is determined at relatively high q range (0.002–0.01 nm^{-1}). The scattering is produced by packing of primary C–S–H gel particles. Volume-fractal scaling works from the R_c length scale up to the correlation length; ξ_v . In this range the mass (solid volume) of C–S–H within radius r of any one point in the structure scales as r^{D_v} where $D_v < 3$. Thus the total volume fraction of the sample occupied by the C–S–H volume-fractal morphology, ϕ_{MAX} , when the solid C–S–H volume fraction of the sample is $\phi_{\text{C-S-H}}$, is given by: $\phi_{\text{MAX}} = \phi_{\text{C-S-H}} (\xi_v/R_c)^{(3-D_v)}$. Thus, within a unit sample volume containing solid C–S–H volume fraction, $\phi_{\text{C-S-H}}$, determined by the model fits, it is expected that the volume taken up by the overall volume fractal morphology (C–S–H solid and pores forming the volume fractal morphology) to have volume fraction, ϕ_{MAX} , (i.e. not clinker grains, large pores, CH, etc.). Note that while $\phi_{\text{C-S-H}}$ is a well-defined model fitting parameter, ϕ_{MAX} , and the ratio, $\phi_{\text{MAX}}/\phi_{\text{C-S-H}}$, is more of rough estimate. For example, if separately-seeded volume-fractal structures grow into each other, this ratio will not be accurate. Within the range $1/\xi_v < q < 1/R_c$, it is expected to observe a volume-fractal power law: $I(q) \sim q^{-D_v}$. For $q < 1/\xi_v$, the volume-fractal scaling ceases and the scattering should become flat with q at low q . However, this is buried under the surface-fractal scattering.

In fitting the data, the need to incorporate R_c with η , and a well-defined single-globule term (in addition to the volume-fractal) in the first bracket of Eq. (A1), is strong evidence for a solid volume-fractal phase. For a spheroid of aspect ratio, β , the form-factor for a single globule, $F^2(q)$, is given by:

$$F^2(q) = \frac{\pi}{2} \left| \Delta \rho^2 V_p^2 \int_0^1 \frac{J_{3/2}(qR_0 [1 + (\beta^2 - 1)X^2]^{1/2})}{(qR_0 [1 + (\beta^2 - 1)X^2]^{1/2})^{3/2}} dX \right|^2 \quad (\text{A2})$$

where $V_p = (4/3\beta\pi R_0^3)$, $J_{3/2}(x)$ denotes a Bessel function of order 3/2, and X is an orientational parameter, here integrated over all orientations of the spheroid with respect to q . Use of a mildly spheroidal globule shape avoids the pronounced Bessel function oscillations for spheres ($\beta = 1$), which can perturb the fit at high q . Satisfactory fits are obtainable with both mildly oblate ($\beta = 0.5$) and mildly prolate ($\beta = 2$) aspect ratios, giving globule sizes equivalent to a 5 nm sphere for cement.

The analysis of intensity versus q at higher values of q is used to determine the association of the surface fractal regime with deposition of hydration products (C–S–H outer product) onto the originally smooth surface of the cement clinker grains. While this structure coexists with the volume-fractal, the scattering associated with it is only observable at lower q ($< 0.02 \text{ \AA}^{-1}$).

It is assumed that the surface-fractal (at least, self-affine) behavior also extends to length scales down to R_c . For smaller roughness dimensions (i.e., the C–S–H globule size) it is assumed that there is no more surface roughness to be found. At roughness scale, ξ_s , it is assumed to look at the geometrically smooth surface area of large pores, etc., that are decorated with C–S–H gel. It is assumed that this “smooth” geometrical surface area to be S_0 , which is fitted by the model. For smaller roughness dimensions, more surface area is observed due to mounds and dips previously not seen at coarser measurement scales. In general $S(r) \sim 1/r^{(D_s-2)}$ where D_s is the surface-fractal exponent. It is expected to observe a surface-fractal power law of $I(q) \sim q^{-(6-D_s)}$ for $1/\xi_s < q < 1/R_c$. However, this is generally a steeper power law than that for the volume fractal; so it gets buried under the volume-fractal at higher q values. Nevertheless, the model can be used to

extrapolate from the smooth surface area, S_0 , to the rough surface area, S_{SF} , using the relation: $S_{SF} = S_0(\xi_S/R_c)^{(D_S-2)}$. Unlike the rough estimate above relating ϕ_{C-S-H} and ϕ_{MAX} , this extrapolation of the surface-fractal model to get S_{SF} from S_0 is reasonably accurate.

The BGD term refers to the incoherent flat background scattering, and it is usually subtracted out of both data and fits for convenience. Finally, by doing Porod fits at high q to get the total surface area, S_T , it can be deduced that the surface area associated with the volume-fractal morphology, S_{VF} , is given by $S_{VF} = S_T - S_{SF}$. If it is further assumed that the local arrangement of C–S–H gel globules is similar for the volume- and surface-fractal morphologies, then it is estimated that the ratio of the surface-fractal to volume-fractal C–S–H volume fractions $\approx S_{SF}/S_{VF}$.

References

- [1] C. Andrade, I. Martínez, M. Castellote, P. Zuloaga, Some principles of service life calculation of reinforcements and in situ corrosion monitoring by sensors in the radioactive waste containers of El Cabril disposal (Spain), *J. Nucl. Mater.* 358 (2006) 82–95.
- [2] R.A. Olson, C.M. Neubauer, H.M. Jennings, Damage to the pore structure of hardened Portland cement paste by mercury intrusion, *J. Am. Ceram. Soc.* 80 (1997) 2454–2458.
- [3] A.W. Harris, M.C. Manning, W.M. Tearle, C.J. Tweed, Testing of models of the dissolution of cements—leaching of synthetic CSH gels, *Cem. Concr. Res.* 32 (2002) 731–746.
- [4] C. Carde, R. François, J.M. Torrenti, Leaching of both calcium hydroxide and CSH from cement paste: modeling the mechanical behavior, *Cem. Concr. Res.* 26 (1996) 1257–1268.
- [5] F.J. Ulm, J.M. Torrenti, F. Adenot, Chemoporoplasticity of calcium leaching in concrete, *J. Eng. Mech.* 125 (1999) 1200–1211.
- [6] J.J. Thomas, H.M. Jennings, A.J. Allen, The surface area of cement paste as measured by neutron scattering: evidence for two CSH morphologies, *Cem. Concr. Res.* 28 (1998) 897–905.
- [7] J.J. Thomas, J.J. Chen, A.J. Allen, H.M. Jennings, Effects of decalcification on the microstructure and surface area of cement and tricalcium silicate pastes, *Cem. Concr. Res.* 34 (2004) 2297–2307.
- [8] A.J. Allen, J.J. Thomas, Analysis of C–S–H gel and cement paste by small-angle neutron scattering, *Cem. Concr. Res.* 37 (2007) 319–324.
- [9] R. Gonzalez-Teresa, V. Morales-Florez, H. Manzano, J.S. Dolado, Structural models of randomly packed tobermorite-like spherical particles: a simple computational approach, *Mater. Constr.* 60 (2010) 7–15.
- [10] D.N. Winslow, The fractal nature of the surface of cement paste, *Cem. Concr. Res.* 15 (1985) 817–824.
- [11] A.J. Allen, R.A. Livingston, Relationship between differences in silica fume additives and fine-scale microstructural evolution in cement based materials, *Adv. Cem. Based Mater.* 8 (1998) 118–131.
- [12] H.M. Jennings, P.D. Tennis, Model for the developing microstructure in Portland cement pastes, *J. Am. Ceram. Soc.* (1994) 3161–3172.
- [13] A.J. Allen, J.J. Thomas, H.M. Jennings, Composition and density of nanoscale calcium-silicate-hydrate in cement, *Nat. Mater.* 6 (2007) 311–316.
- [14] J.J. Thomas, A.J. Allen, H.M. Jennings, Density and water content of nanoscale solid C–S–H formed in alkali-activated slag (AAS) paste and implications for chemical shrinkage, *Cem. Concr. Res.* 42 (2012) 377–383.
- [15] A. Trapote-Barreira, J. Cama, J.M. Soler, Dissolution kinetics of C–S–H gel. Flow-through experiments, *Phys. Chem. Earth* 70–71 (2014) 17–31.
- [16] R.A. Young, The Rietveld Method, International Union of Crystallography, Oxford University Press, 1995.
- [17] A.C. Lasaga, Kinetic Theory in the Earth Sciences, Princeton University Press, Princeton, 1998.
- [18] J.R. Barrante, Applied Mathematics for Physical Chemistry, Prentice-Hall, 1974.
- [19] I. Klur, B. Pollet, J. Virlet, A. Nonat, CSH structure evolution with calcium content by multinuclear NMR, Nuclear Magnetic Resonance Spectroscopy of Cement-based Materials, Springer, Berlin Heidelberg, 1998, pp. 119–141.
- [20] D. Massiot, F. Fayon, M. Capron, I. King, S. Le Calve, B. Alonso, G. Hoatson, Modelling one- and two-dimensional solid-state NMR spectra, *Magn. Reson. Chem.* 40 (2002) 70–76.
- [21] C.J. Glinka, J.G. Barker, B. Hammouda, S. Kreuger, J.J. Moyer, W. Orts, The 30 m small-angle neutron scattering instruments at the National Institute of Standards and Technology, *J. Appl. Crystallogr.* 31 (1998) 430–445.
- [22] W. Bumrongjaroen, R.A. Livingston, D.A. Neumann, A.J. Allen, Characterization of fly ash reactivity in hydrating cement by neutron scattering, *J. Mater. Res.* 24 (2009) 2435–2448.
- [23] J.J. Thomas, H.M. Jennings, A.J. Allen, Relationships between Composition and density of tobermorite, jennite, and nanoscale CaO–SiO₂–H₂O, *J. Phys. Chem. C* 114 (2010) 7594–7601.
- [24] J. Ilavsky, P.R. Jemian, Irena: tool suite for modeling and analysis of small-angle scattering, *J. Appl. Crystallogr.* 42 (2009) 347–353.
- [25] J.W. Carey, P.C. Lichtner, Calcium silicate hydrate (CSH) solid solution model applied to cement degradation using the continuum reactive transport model FLOTRAN, Transport Properties and Concrete Quality: Materials Science of Concrete, 2007, pp. 73–106.
- [26] J.W. Carey, P.C. Lichtner, Calcium silicate hydrate solid solution model applied to cement degradation using the continuum reactive transport model FLOTRAN, Report LA-UR-06-0636, 2006.
- [27] J.J. Thomas, H.M. Jennings, A.J. Allen, Determination of the neutron scattering contrast of hydrated Portland cement paste using H₂O/D₂O exchange, *Adv. Cem. Based Mater.* 7 (1998) 119–122.
- [28] A.J. Allen, R.C. Oberthur, D. Pearson, P. Schofield, C.R. Wilding, Development of the fine porosity and gel structure of hydrating cement systems, *Philos. Mag. B* 56 (1987) 263–288.
- [29] A.J. Allen, A.H. Baston, C.R. Wilding, Small angle neutron scattering studies of pore and gel structures, diffusivity, permeability and damage effects, *Mater. Res. Soc. Symp. Proc.* 137 (1989) 119–125.
- [30] P.D. Tennis, H.M. Jennings, A model for two types of calcium silicate hydrate in the microstructure of Portland cement pastes, *Cem. Concr. Res.* 30 (2000) 855–863.
- [31] V. Morales-Florez, N. Findling, F. Brunet, Changes on the nanostructure of cementitious calcium silicate hydrates (C–S–H) induced by aqueous carbonation, *J. Mater. Sci.* 47 (2012) 764–771.
- [32] H.M. Jennings, A model for the microstructure of calcium silicate hydrate in cement paste, *Cem. Concr. Res.* 30 (2000) 101–116.
- [33] J.J. Thomas, A.J. Allen, H.M. Jennings, Structural changes to the calcium-silicate-hydrate gel phase of hydrated cement with age, drying, and resaturation, *J. Am. Ceram. Soc.* 91 (2008) 3362–3369.
- [34] J. Zarzycki, Fractal properties of gels, *J. Non-Cryst. Solids* 95 (1987) 173–184.
- [35] D.A. Kulik, M. Kersten, Aqueous solubility diagrams for cementitious waste stabilization systems: II, end-member stoichiometries of ideal calcium silicate hydrates solid solutions, *J. Am. Ceram. Soc.* 84 (2001) 3017–3026.
- [36] W. Chiang, E. Fratini, P. Baglioni, D. Liu, S. Chen, Microstructure determination of calcium-silicate-hydrate globules by small-angle neutron scattering, *J. Phys. Chem. C* 116 (2002) 5055–5061.
- [37] D. Sen, S. Mazumder, S. Tarafdar, Pore morphology and pore surface roughening in rocks: a small-angle neutron scattering investigation, *J. Mater. Sci.* 37 (2002) 941–947.
- [38] E. Cappelletto, S. Borsacchi, M. Geppi, F. Ridi, E. Fratini, P. Baglioni, Comb-shaped polymers as nanostructure modifiers of calcium silicate hydrate: a ²⁹Si solid-state NMR investigation, *J. Phys. Chem. C* 117 (2013) 22947–22953.
- [39] H.F. Taylor, Proposed structure for calcium silicate hydrate gel, *J. Am. Ceram. Soc.* 69 (1986) 464–467.
- [40] C. Plassard, E. Lesniewska, I. Pochard, A. Nonat, Investigation of the surface structure and elastic properties of calcium silicate hydrates at the nanoscale, *Ultramicroscopy* 100 (2004) 331–338.
- [41] J.J. Chen, J.J. Thomas, H.F. Taylor, H.M. Jennings, Solubility and structure of calcium silicate hydrate, *Cem. Concr. Res.* 34 (2004) 1499–1519.
- [42] R.J. Myers, S.A. Bernal, R. San Nicolas, J.L. Provis, Generalized structural description of calcium-sodium aluminosilicate hydrate gels: the cross-linked substituted tobermorite model, *Langmuir* 29 (2013) 5294–5306.